Feasibility of Estimating Ice Sheet Internal Temperatures Using Ultra-Wideband Radiometry

Yuna Duan, Caglar Yardim[®], *Member, IEEE*, Michael Durand[®], Kenneth C. Jezek[®], Joel T. Johnson[®], *Fellow, IEEE*, Alexandra Bringer[®], Shurun Tan[®], *Member, IEEE*, Leung Tsang[®], *Life Fellow, IEEE*, and Mustafa Aksoy[®], *Member, IEEE*

Abstract-Although ice sheet internal temperature is a first-order control on glacier dynamics, relatively few in situ borehole temperature profiles exist. The ultra-wideband softwaredefined microwave radiometer (UWBRAD) was designed to estimate internal ice sheet temperature (T_i) by measuring microwave brightness temperatures (T_h) from 0.5 to 2 GHz. The retrieval of T_i from T_b is not straightforward, however, due in part to the complicating effects of ice density fluctuations on T_b . In this article, we report a simulation study to assess the feasibility of realizing three science goals: the retrieval of: 1) T_i at 10 m depth to within 1 K; 2) vertically averaged T_i to within 1 K; and 3) the vertical T_i profile to within 1 K RMSE. Two analyses along the Greenland ice divide are presented. First, we assess the ideal UWBRAD T_i retrieval precision via the Cramér-Rao lower bound (CRLB). Second, we perform a "virtual experiment" (VE) using synthetic UWBRAD observations. Both the CRLB and VE analyses indicate that the science goals are achievable with the caveats that ice thickness and UWBRAD T_b precision impact performance. Assuming a UWBRAD T_b precision of 0.5 K, and for places where ice sheet thickness is less than 3 km, all science goals can be achieved. The results of the study provide a strong indication of the potential of UWBRAD to provide valuable Greenland ice temperature profile information to the scientific community.

Index Terms—Bayesian, ice sheet, microwave radiometry, temperature.

I. INTRODUCTION

TCE sheet internal temperature (T_i) is an essential factor for understanding glacier dynamics and predicting future changes of glacier ice. However, temperature borehole data are relatively scarce. Spaceborne and airborne remote sensing instruments characterize most of the important variables necessary to understand current ice sheet behaviors and to predict future changes. Derived geophysical quantities include

Manuscript received 8 November 2021; revised 27 May 2022; accepted 14 July 2022. Date of publication 22 September 2022; date of current version 18 November 2022. This work was supported in part by the National Aeronautics and Space Administration (NASA) Instrument Incubator under Grant NNX14AE68G and in part by the Cryospheric Science Programs under Grant 80NSSC18K0550 and Grant NNX14AH91G. (Corresponding author: Caglar Yardim.)

Yuna Duan, Michael Durand, and Kenneth C. Jezek are with the School of Earth Science and the Byrd Polar and Climate Research Center, The Ohio State University, Columbus, OH 43210 USA (e-mail: duan.138@osu.edu; durand.8@osu.edu).

Caglar Yardim, Joel T. Johnson, Alexandra Bringer, and Mustafa Aksoy are with the Department of Electrical and Computer Engineering, The Ohio State University, Columbus, OH 43210 USA (e-mail: yardim.7@osu.edu).

Shurun Tan and Leung Tsang are with the Department of Electrical Engineering and Computer Science, University of Michigan, Ann Arbor, MI 48109 USA.

Digital Object Identifier 10.1109/TGRS.2022.3208754

ice sheet surface elevation change, mass change, ice sheet thickness, surface accumulation rate, internal layer stratigraphy, seaward bathymetry, and basal geology [1]. At present, internal ice sheet temperature is absent from this list. Temperatures at 10 m depth are characteristic of mean-annual surface-temperature and are recognized as an important climate monitoring parameter [2]. Consequently, ice temperature information is important for monitoring the regional climate and is fundamental for understanding changes in ice sheet mass balance and dynamics. Glacier deformation rates are significantly affected by the thermal status of the constituent ice because the stiffness of ice is temperature dependent.

Jezek et al. [3] describe a radiometric approach for measuring ice sheet temperature via multispectral low-frequency microwave emission measurements. Preliminary work by [4] using soil moisture and ocean salinity mission (SMOS) L-band data to retrieve Antarctica internal ice sheet temperatures demonstrated that the approach is promising. By examination of measurements of SMOS, it showed clear evidence of the influence of deeper subsurface emissions [5]. Because the brightness temperature of an ice sheet results from a combination of emission, attenuation, and scattering effects from many internal ice sheet layers, the retrieval of even depth-averaged temperatures from a single frequency brightness temperature alone is challenging. The use of multiple frequencies provides measurements in bands which are influenced by particular properties (scattering for example) to differing degrees and with varying penetration. The approach capitalizes on the fact that over the frequency range 0.5-2 GHz, penetration depths are large, ranging from 500 to 3000 m or more [6]. Following concepts from atmospheric temperature sounding [7], measurements of upwelling microwave radiation at higher frequencies corresponds to microwave radiation emanating from ice nearer to the ice sheet surface. Similarly, emissions at lower frequencies upwell from deeper within the ice column. Measuring emissions across a range of frequencies thus provides the potential for inference of ice temperature vertical profiles.

The ultra-wideband software-defined microwave radiometer (UWBRAD) funded by the NASA Instrument Incubator Program (IIP) is designed to measure low-frequency microwave emissions [8], [9]. UWBRAD was designed to provide nadirial brightness temperature observations from 0.5 to 2 GHz using multiple frequency channels. Because this frequency range is not a protected portion of the spectrum, UWBRAD must allow for brightness temperature measurements in the presence of other, man-made, radio frequency interference (RFI). The goal is achieved by sampling the 0.5–2 GHz frequency range into

1558-0644 © 2022 IEEE. Personal use is permitted, but republication/redistribution requires IEEE permission. See https://www.ieee.org/publications/rights/index.html for more information.

12–88 MHz bandwidth frequency channels so that advanced RFI detection and mitigation methods can be applied in real time. Brightness temperatures within each 88 MHz bandwidth channel are further resolved at a frequency resolution of 0.24 MHz, allowing both the detection and filtering of interference as well as use as a "hyperspectral" radiometer for specific applications. This process enables UWBRAD to identify open portions of the spectrum that can be used for radiometric observations even in the presence of other transmitting sources.

In this study, we assess the feasibility of inferring ice temperature from UWBRAD. The principal challenge with this problem is overcoming the confounding effects of ice density variations on the microwave signal. Tan et al. [6] explored the impact of ice density variations on microwave emission at UWBRAD frequencies. Essentially, limited knowledge in ice density degrades the ability to infer ice sheet temperatures. Such confounding factors (also known as "nuisance parameters") are commonplace in retrieval problems, and often require careful consideration to mitigate their impact on retrieval performance. The specific science goals over the Greenland Ice Sheet and the reason for setting up these goals are as follows.

- 1) Retrieval of T_i at 10 m depth to within 1 K. 10 m temperatures approximate the mean annual temperature and so it represents an important climate parameter [2].
- 2) Retrieval of vertically averaged T_i to within 1 K. Spatial variations in average temperature can be used as a proxy for improving temperature-dependent ice-flow models.
- 3) Retrieval of vertical T_i profile to within 1 K RMSE. Remote sensing measurements of temperature-depth profiles can substantially improve ice flow models.

We assess the feasibility of achieving the three science goals by presenting two analyses along the Greenland ice divide. First, we assess the ideal UWBRAD T_i precision via the Cramér-Rao lower bound (CRLB). Second, we perform a "virtual experiment" (VE) using synthetic UWBRAD brightness temperature (T_h) observations. In the context of the VE, we present a Bayesian Markov chain Monte Carlo (MCMC) approach for temperature profile retrieval. These two analyses complement each other: the CRLB is the best possible precision realizable in theory, given the sensitivity of the observables to the quantities being estimated; however, it does not guarantee that such a solution can be realized. The VE demonstrates retrieval with a particular algorithm, but (in isolation from the CRLB) is more susceptible to misinterpretation. A successful realization of scientific goals from both the UWBRAD and VE analyses (as is demonstrated in what follows) supports ongoing retrieval efforts with UWBRAD measured data, as will be reported in subsequent publications.

II. STUDY AREA AND DATASETS

A. Study Area

The assumed flight path for UWBRAD in Greenland that is considered in the simulation study is shown in Fig. 1, and stretches from American Thule Air Force Base in northwestern Greenland along the ice divide (as illustrated by the flow lines [10] in Fig. 1) south to Crete station, and then southwest to Sondestrom Air Base. This flight path was chosen to overlap existing locations where ice cores exist, providing

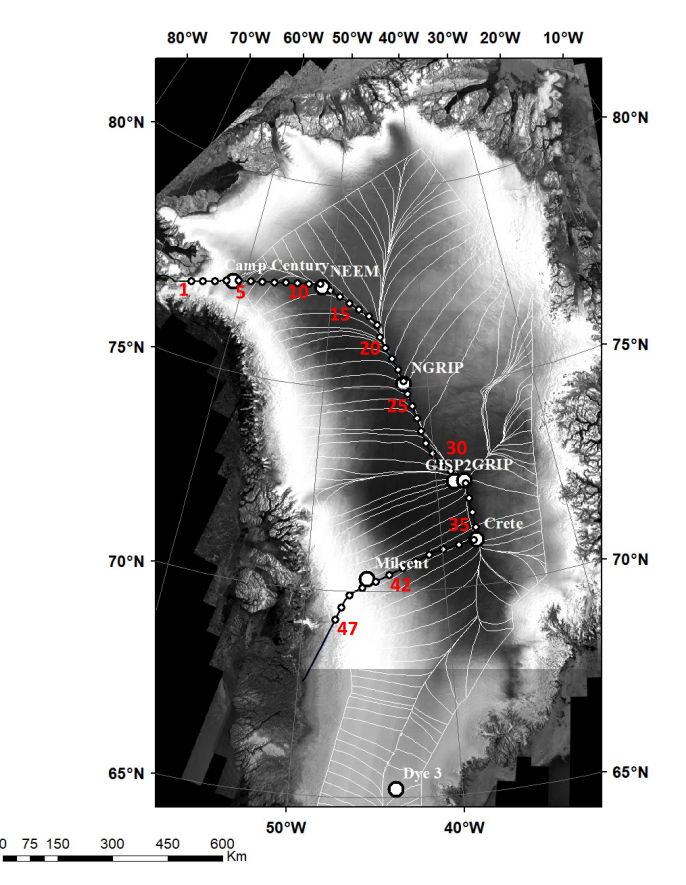


Fig. 1. Nominal flight path of the UWBARD airborne experiment overlaid on a Radarsat-1 [11] mosaic image of Greenland. All analyses in this study are performed along the flight line. White lines indicate the ice flow. Small circles are the 47 waypoints used for synthetic experiments.

temperature validation data; eight deep ice core sites are covered. Moreover, temperature retrieval along the ice divide is relatively simpler than at other locations because: 1) horizontal ice advection is minimized, simplifying the ice temperature modeling and 2) the snow and firn are dry, minimizing the influence of liquid water on the microwave emission. The simulated flight path covers 1674 km, divided into 47 waypoints roughly separated by 36 km for CRLB and VE analyses.

B. Datasets

A model of ice sheet internal temperature T_i is used in both the CRLB and VE analyses and is described in detail in Section III. Datasets to drive the ice temperature model include: 1) ice sheet surface temperature from the regional atmospheric climate model (RACMO) [12], a multidecadal average of the monthly reanalysis data; 2) snow accumulation rate, also from RACMO, obtained similar to surface temperature; 3) ice sheet thickness from Operation Ice Bridge (OIB) measurements [13]; and 4) geothermal heat flux from satellite magnetic data [14], available as a gridded dataset for the Community Ice Sheet Model (CISM) via [15]. Plots of all these quantities at the 47 points along the nominal path are shown in Fig. 2.

The T_i model assumes a steady state temperature profile; to examine the effect of this assumption on our analysis, we make use of the T_i vertical profile measured via the GISP2 ice core [16], [17].

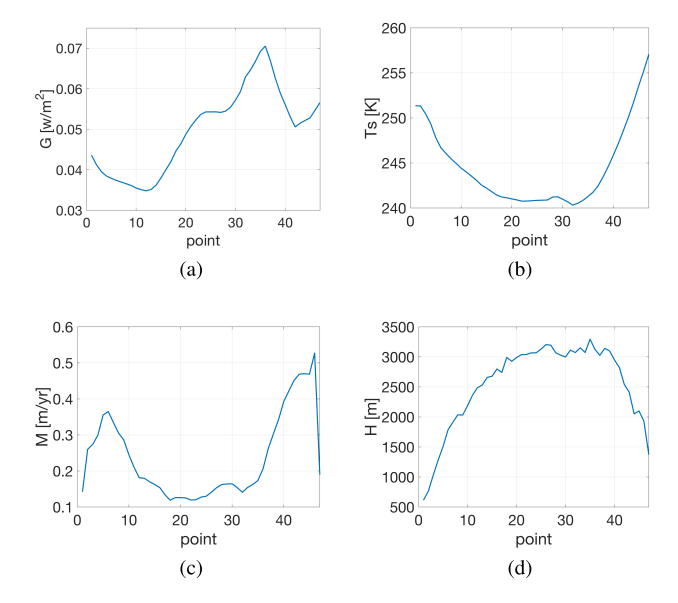


Fig. 2. Traces of the four input parameters related to modeling ice sheet temperature along the flight path. (a) Geothermal heat flux. (b) Surface temperature. (c) Snow accumulation rate. (d) Ice thickness.

We further use borehole measurements of ice density from Summit station [18] (located near GRIP in Fig. 1) to represent the average ice density with depth, and neutron probe measurements [19], [20] of density from T41 station near Summit to assist in the modeling variations of ice density at centimetric spatial scales. These ice density fluctuations play in important role in microwave emission, as discussed below.

III. METHODS

In both the VE and CRLB analyses, two models are used to relate the synthetic T_b observations to the T_i vertical profiles: an ice temperature model based upon 1-D heat flow (Section III-A) and a radiative transfer model (RTM) that links vertical profiles of T_i and nuisance parameters with microwave emission (Section III-B). Section III-C describes the statistical model of vertical density fluctuations that represents our treatment of the nuisance parameters. The CRLB and VE analyses are then described in Sections III-D and III-E, respectively.

A. Ice Sheet Temperature Model

In general, ice sheet temperatures are highly dynamic vertically, governed at the surface by diurnal and interannual meteorological variations, governed at the base by geothermal heat and frictional heating from basal slip, and by the advection of heat laterally along glacier flow paths. In this study, we estimate only temperature at 10 m and greater, where temporal fluctuations are governed by long-term climate rather than short-term meteorological processes. Moreover, we limit our analyses to locations along the Greenland ice divide, where advection is minimal, as is heating due to ice deformation. Thus, in this exploratory study, we use a simple 1-D steady state heat-flow model by Robin [21] to calculate the vertical temperature profile. Because horizontally advected heat is excluded, the model is only applicable over the ice divide, where there is negligible horizontal ice movement. Given the surface temperature (T_s) in [K], ice sheet thickness (H) in [m],

snow accumulation rate (M) in [m/yr], and geothermal heat flux (G) in $[w/m^2]$, the Robin model describes steady-state temperatures T(z) in [K] as a function of elevation z above the ice sheet base as

$$T(z) - T_s = \frac{-G\sqrt{\pi}}{2\kappa q} [\operatorname{erf}(zq) - \operatorname{erf}(Hq)]$$

$$q^2 = \frac{M}{2\kappa H}$$
(1)

where $K = 45 \text{ m}^2/\text{yr}$ is the ice thermal diffusivity and $\kappa = 2.7 \text{ W/m} \cdot \text{K}$ is the ice thermal conductivity [22], [23].

Note that the temperature at the bottom of the ice sheet decouples from geothermal heat flux if the base of the ice sheet is melting and the model above would need to be adjusted. However, the base along the ice divide is mostly frozen [24]. Therefore, this study uses a model without any basal melting.

B. Radiative Transfer Model

The prediction of microwave emission from firn at 0.5–2.0 GHz is an active area of research. Tan et al. [6] presented a coherent model of emission in the context of the UWBRAD mission. They argue that in the UWBRAD frequency range, the ice particle grain size will be relatively small compared with the wavelength of microwave radiation, and thus volume scattering can be ignored. They also demonstrate that coherent superposition of electromagnetic (EM) waves, controlled by variations in density, may be an important factor in determining T_b spectra at these frequencies. However, coherent model computations are relatively time consuming, requiring a large number of statistical realizations of the density profile. Thus, in these studies, we use a modified version of the coherent model [25], referred to as the "partially-coherent model." By assuming that coherent effects can be considered only between adjacent sections of firn, the total number of computations and thus run time is significantly reduced. Refer to [6] for further details on the model. The RTM uses the temperature and density profiles as inputs. Due to the stochastic model used for density fluctuations, an average over realizations is required to predict the expected average brightness temperature. The T_b results shown in what follows were obtained by averaging over 500 realizations.

C. Density Profile Model

Brogioni et al. [26] showed that density fluctuations in the upper part of the ice sheet strongly influence L-band brightness temperatures. Following [27], we model density as the sum of a mean density profile and fluctuating terms, using the two data sources from Summit station described previously

$$\rho(d) = \bar{\rho}(d) + \rho_n(d) \tag{2}$$

where d = z - H is the depth relative to the surface of an ice sheet with thickness H. The unit for all parts of the density is g/cm^3 . We assume the mean density profile with depth $\bar{\rho}(d)$ increases exponentially and is obtained by curve-fitting the density data in [20]

$$\bar{\rho}(d) = 0.917 - 0.55 \times e^{-0.236d}$$
. (3)

The density fluctuations ρ_n are assumed to follow a multivariate normal distribution exhibiting vertical autocorrelation and

zero mean [6], [28]. The covariance of ρ_n between two points d and d', $C_{\rho}(d, d')$ is given by

$$C_{\rho}(d, d') = \Delta^2 e^{-d\alpha^{-1}} e^{-|d-d'|l_c^{-1}}.$$
 (4)

Thus, the variance of ρ_n decreases exponentially with distance below the surface, with the scale factor α , standard deviation at surface of Δ in kg/m³ and correlation length l_c in meters.

D. Cramér-Rao Lower Bound

The CRLB provides a limit to achievable performance for a given estimation problem: i.e., given the set of models and geophysical datasets described previously, the CRLB represents the smallest achievable uncertainty variance in an estimate of ice temperatures.

Define the vector of radiometer measurements at N frequencies $\{f_i\}_{i=1}^N$ as \mathbf{y} . The environmental model vector \mathbf{x} consists of the set of unknown parameters that drive both the ice temperature model and the density model. Receiver noise not related to the ice emissions is represented by the vector \mathbf{n} across all frequencies. Assuming an additive zero-mean Gaussian noise, it is possible to write the problem as

$$\mathbf{x} = [T_s \ H \ M \ G \ \alpha \ \Delta \ l_c]^T \tag{5}$$

$$\mathbf{y} = [y_{f_1} \ y_{f_2}, \dots, y_{f_N}]^T \tag{6}$$

$$\mathbf{y} = f(\mathbf{x}) + \mathbf{n}.\tag{7}$$

T superscript here indicates the matrix transpose operation with all other parameters assumed known. Given this problem formulation, the likelihood function is given by

$$\mathcal{L}(\mathbf{x}) = p(\mathbf{y}|\mathbf{x}) = (2\pi)^{-N/2} |\mathbf{C}|^{-1/2}$$

$$\times \exp\left[-\frac{(\mathbf{y} - f(\mathbf{x}))^T \mathbf{C}^{-1} (\mathbf{y} - f(\mathbf{x}))}{2}\right] \quad (8)$$

where C is the noise covariance matrix. The Fisher information matrix (FIM) for this problem can then be computed using [29]

$$\mathbf{FIM}_{ij}(\mathbf{x}) = -E \left\{ \frac{\partial \ln p(\mathbf{y}|\mathbf{x})}{\partial \mathbf{x}_i} \frac{\partial \ln p(\mathbf{y}|\mathbf{x})}{\partial \mathbf{x}_j} \right\}$$
$$= -\int \frac{\partial^2 \ln p(\mathbf{y}|\mathbf{x})}{\partial \mathbf{x}_i \partial \mathbf{x}_i} p(\mathbf{y}|\mathbf{x}) d\mathbf{x}$$
(9)

where each entry in the FIM corresponds to the *i*th and *j*th environmental parameters \mathbf{x}_i and \mathbf{x}_j , and $E\{\cdot\}$ is the expected value. As shown by [29], for the additive Gaussian noise case, the FIM can be computed by

$$\mathbf{FIM}(\mathbf{x})_{ij} = \left[\frac{\partial f(\mathbf{x})}{\partial \mathbf{x}_i}\right]^T \mathbf{C}^{-1}(\mathbf{x}) \left[\frac{\partial f(\mathbf{x})}{\partial \mathbf{x}_j}\right] + \frac{1}{2} \text{tr} \left[\mathbf{C}^{-1}(\mathbf{x}) \frac{\partial \mathbf{C}(\mathbf{x})}{\partial \mathbf{x}_i} \mathbf{C}^{-1}(\mathbf{x}) \frac{\partial \mathbf{C}(\mathbf{x})}{\partial \mathbf{x}_i}\right]$$
(10)

where tr is the trace. The rms error any unbiased estimator $\widehat{\mathbf{x}}$ can achieve is thus bounded by the CRLB, which is the inverse of the FIM

$$\operatorname{var}(\widehat{\mathbf{x}}) = E\left\{ (\widehat{\mathbf{x}} - \mathbf{x}) (\widehat{\mathbf{x}} - \mathbf{x})^T \right\} \ge \mathbf{CRLB} = \mathbf{FIM}^{-1}.$$
 (11)

The CRLB is calculated for the seven parameters used in the forward model. The CRLB of the temperature at any height can then be obtained from the 7×7 CRLB matrix

$$\mathbf{CRLB}(T(z)) = \left[\frac{\partial T(z)}{\partial \mathbf{x}}\right] \mathbf{CRLB}(\mathbf{x}) \left[\frac{\partial T(z)}{\partial \mathbf{x}}\right]^{T}$$
(12)

where T(z) is defined as in (1). The partial derivatives of T(z) with respect to the input parameters are given by

$$\frac{\partial T(z)}{\partial T_{s}} = 1, \quad \frac{\partial T(z)}{\partial l_{c}} = \frac{\partial T(z)}{\partial \alpha} = \frac{\partial T(z)}{\partial \Delta} = 0 \tag{13}$$

$$\frac{\partial T(z)}{\partial G} = \frac{1}{k_{c}} \sqrt{\frac{\pi H k_{d}}{2M}} \left[\operatorname{erf} \left(z \sqrt{\frac{M}{2k_{d}H}} \right) - \operatorname{erf} \left(H \sqrt{\frac{M}{2k_{d}H}} \right) \right] \tag{14}$$

$$\frac{\partial T(z)}{\partial M} = \frac{G}{k_{c} \sqrt{8k_{d}HM}}$$

$$\times \left[\frac{-k_{d}H\sqrt{\pi}}{M} \left(\operatorname{erf} \left(z \sqrt{\frac{M}{2k_{d}H}} \right) \right) - \operatorname{erf} \left(H \sqrt{\frac{M}{2k_{d}H}} \right) \right]$$

$$- \operatorname{erf} \left(H \sqrt{\frac{M}{2k_{d}H}} \right) \right]$$

$$- H \exp \left(-H^{2} \frac{M}{2k_{d}H} \right)$$

$$- \operatorname{erf} \left(H \sqrt{\frac{M}{2k_{d}H}} \right) - z\sqrt{\pi} \exp \left(-z^{2} \frac{M}{2k_{d}H} \right)$$

$$- \operatorname{erf} \left(H \sqrt{\frac{M}{2k_{d}H}} \right) - z\sqrt{\pi} \exp \left(-z^{2} \frac{M}{2k_{d}H} \right)$$

$$- \operatorname{erf} \left(H \sqrt{\frac{M}{2k_{d}H}} \right) - z\sqrt{\pi} \exp \left(-z^{2} \frac{M}{2k_{d}H} \right)$$

$$- \operatorname{erf} \left(H \sqrt{\frac{M}{2k_{d}H}} \right) \right].$$

$$(16)$$

This enables projection of the uncertainties of the inverted parameters \mathbf{x} into those of the temperature at any location along the flight path and depth.

E. Virtual Experiment

As noted above, the CRLB only provides a theoretical lower limit for precision that an ice temperature estimator can achieve, but it does not guarantee that a practical estimator with estimator variance close to CRLB exists. Thus, we also present a VE in which we produce synthetic observations and apply a retrieval algorithm to estimate ice temperatures. Here we use a MCMC retrieval algorithm to estimate ice sheet temperature and density model parameters. The MCMC is a method for obtaining a sequence of random samples from a probability distribution for which direct sampling is difficult or impossible. It works by generating a sequence of sample values in such a way that, as more and more sample values are produced, the distribution of values more closely approximates the desired distribution. In this study, we use the Metropolis algorithm [30].

MCMC sample values are produced iteratively, with the distribution of the next sample being dependent only on the current sample value. Specifically, at each iteration, the algorithm picks a candidate for the next sample value based on the current sample value. Then, with some probability, the candidate is either accepted (in which case the candidate value is used in the next iteration) or rejected (in which case the candidate value is discarded, and the current value is reused in the next iteration).

Among the parameters involved in modeling T_b , the geothermal heat flux G and the standard deviation of the density fluctuation Δ are arguably the most highly uncertain ones.

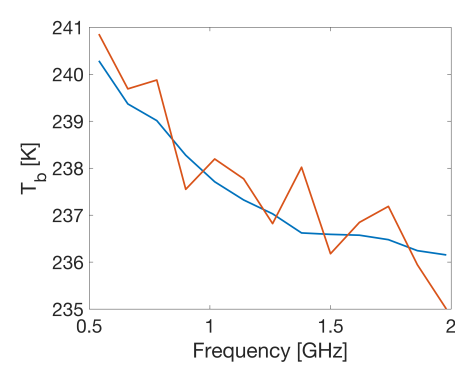


Fig. 3. Forward simulation (blue line) and UWBRAD synthetic observation (red line) with 0.5 K noise added to the forward simulation for the Crete waypoint along the flight path.

The surface temperature T_s , though can be attained in various way, is influential for the ice temperature profile. So they were treated as unknown in the VE. For each one of the 47 points selected along the flight path, synthetic UWBRAD measurements were generated via the RTM with a specific set of T_s , G, and Δ , where $\overline{T_s} = T_{\text{RACMO}} + 1$, $G = G_{\text{CISM}}$, $\Delta = 30 \text{ kg/m}^3$, $\alpha = 70$, and $l_c = 0.4 \text{ m}$. Stochastic density parameters were computed from the density profile provided by Morris [20]. RACMO temperatures are modified to match the moderate resolution imaging spectroradiometer (MODIS) values. Gaussian white noise with a standard deviation of 0.5 K (nominal case) is then added to the simulated T_b . We explore sensitivity to various noise levels below. The synthetic observation near Crete (waypoint 35) along the flight path is illustrated in Fig. 3 as a show case.

In this study, we assume uniform estimates of these parameters (prior), with parameter ranges as follows.

- 1) $T_s = \overline{T_s} + dT_s$ with $-3 < dT_s < 3$ K.
- 2) $0.03 < G < G_{\text{melt}} \text{ W/m}^2$.
- 3) $20 < \Delta < 60 \text{ kg/m}^3$.

Where $G_{\rm melt}$ is the maximum value that G can take without the base temperature exceeding the melt temperature. dT_s is selected based on previous study of MODIS T_s offset from actual T_s measurements [31]. We constructed separate Markov Chains for each point along the flight path, based on the priors and synthetic observations. We then computed estimates of each of the forward statistics based on the MCMC chain. We computed a temperature profile estimate based on the estimated parameters.

Forward model itself uses a large number of stochastic realizations for generating stable T_b (500 realizations were used in this study; see Section III-B) computation. Hence, running the RTM at each step of the MCMC chain is computationally expensive. A lookup table of size $5 \times 5 \times 5$ for each parameter was therefore generated to improve computation efficiency. At each step, the T_b is evaluated by 3-D interpolation within the lookup table.

F. Analyses

To demonstrate feasibility, we perform several CRLB and VE experiments, varying the observation uncertainty, which represents the expected level of noise in the UWBRAD observations. This investigation of sensitivity of the analyses to input parameters studies the likelihood of achieving science goals. Both CRLB and VE are computed across a range of

assumptions regarding UWBRAD T_b observation precision, from 0.5 to 5.0 K. We also perform the CRLB analysis with several of the UWBRAD channels removed, to ascertain the effect of losing information in one of the channels due to RFI. We use the MCMC to explore the correlation between the parameter estimates across the Markov chains, which explores the uniqueness of the solutions. Finally, we use the MCMC to explore the effect of the simple Robin T_i model in the retrieval. We do this by constructing a separate experiment where we simulate the UWBRAD T_b data using borehole T_i data, perform retrieval using the Robin model as usual, and compare retrieved and borehole T_i values.

IV. RESULTS

A. CRLB Analyses

- 1) Forward Model Parameter Estimates: The square roots of CRLB for the seven parameters used in the forward model are given in Fig. 4. The standard deviation of each parameter is computed from the square root of the diagonal entries of the CRLB matrix ($\sigma_i = (\mathbf{CRLB}(i, i))^{1/2}$). As expected, the results given in Fig. 4 showed increased rms error with increasing measurement noise. Thus, the results for a noise value of 0.5 K are indicative of the best performance that can be expected from the inversion. For a noise value of 0.5 K, Fig. 4 shows that the surface temperature can be obtained with a standard deviation of 0.8 K while the ice thickness can be estimated with accuracy no better than 36 m. Geothermal heat flux and accumulation rate can be estimated with standard deviation values at $T_n = 1$ K better than 0.005 W/m² and 0.05 m/yr, respectively. The other parameters that characterized density fluctuations are also estimated well using the UWBRAD system. It is important to note that neither the partially coherent RTM nor the Robin temperature models are suitable at the beginning and the end of the flight path that include ablation and wet ice zones. The current simulations show UWBRAD capabilities if the assumed models hold along the entire flight path.
- 2) Vertical Temperature Profile Estimates: The square root of CRLB for the vertical profiles of T_i along the path are provided in Fig. 5 with a noise level of 1 K. The standard deviation is less than or around 1 K for most of the ice sheet along the flight path, although there are a few regions where the standard deviation goes up to 6 K. The overall mean value is 1.3 K and the average standard deviation at 10 m depth along the flight path is 0.9 K.
- 3) CRLB With RFI: Due to the ultra-wideband nature of the method, instruments operating at L-band frequencies will encounter numerous RFI sources operating at different frequencies. Here, theoretical limits of the system are explored when one or more channels are lost. The CRLB values with varying number of channels are shown in Fig. 6. The CRLB values will vary for simulations that use less than all 12 channels, depending on which channel(s) is/are lost. The best and worst performing scenarios, and the average of all possible scenarios are plotted as min, max, and average CRLB. As expected, the performance of the system degrades when using a smaller number of channels. However, even for UWBRAD operating with only ten frequency channels, the CRLB values remain similar to those for the full 12-channel

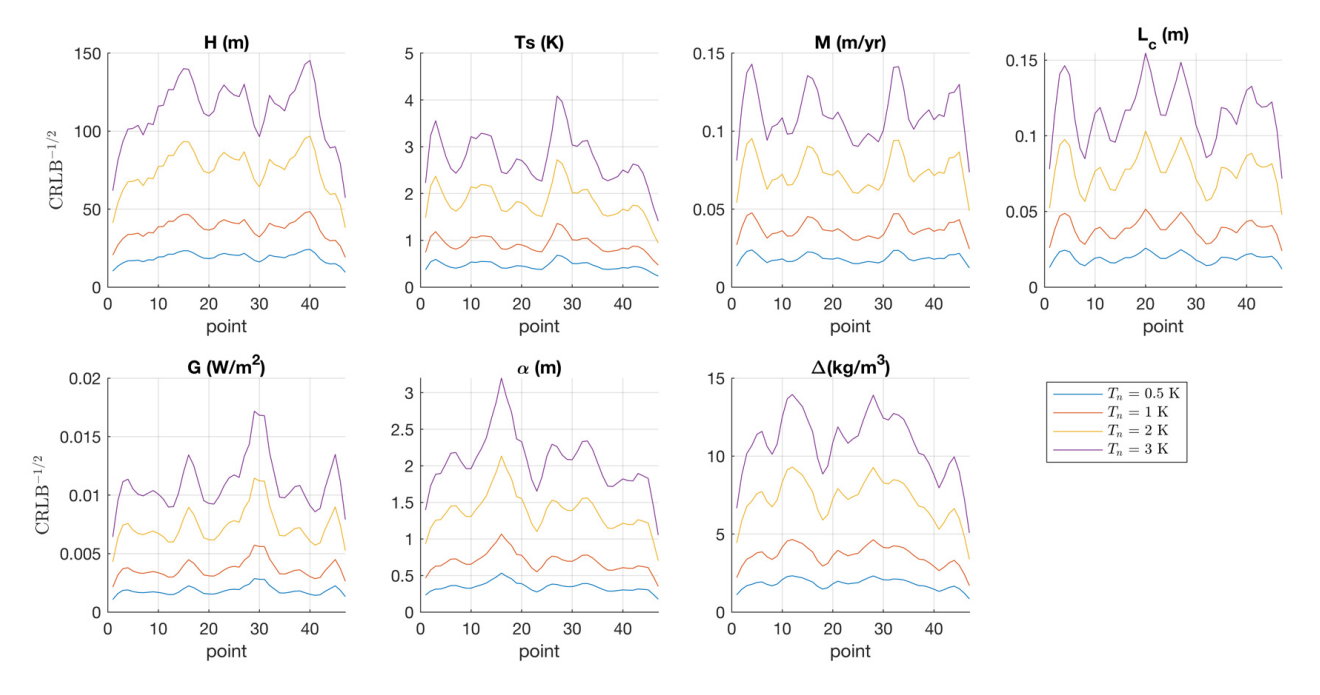


Fig. 4. Square root of the CRLB of ice sheet parameters along the track with varying noise temperatures.

system. The degradation in performance however rapidly increases with further reduction in the number of frequencies used. For cases with less than nine channels, the selection of which frequencies are lost becomes important, with the large gap between the max, mean, and minimum standard deviation values obtained from the CRLB. The surface temperature mean rms error increases from 0.8 to 2 K for example when four frequencies are not used, while the error sharply increases to 8 K when another frequency is lost.

One thing to mention is that each frequency provides information on physical temperature for different depths of the ice sheet. Retrieval success depends upon having a range of high and low frequencies: having eight frequencies evenly spread across the frequency range is likely to be more successful than the eight highest frequencies. Thus, we cannot assess the value of each individual channel.

B. Virtual Experiment Analyses

1) Forward Model Parameter Estimates: For each point, the estimations of each parameter in the VE compared with the truth and the prior are shown in Fig. 7. In Fig. 7(a) and (b), the estimation of density variation and surface temperature are improved toward the true value after the MCMC process for 44 out of 47 cases. The main reason for the incorrect results is the highly nonlinear and complex cost function surface with a large number of local minima in addition to the global minima. As we are interested in the temperature profile, the density parameters are nuisance parameters. However, they need to be correctly computed simultaneously with the temperature Robin parameters and this increases the dimensions of the search space and sometimes causes the inversion algorithm to get stuck in a local minima. This issue and how to design robust estimators that can mitigate this problem are discussed in detail in [32].

In Fig. 7(c), the prior error in geothermal heat flux can only be partially corrected at the beginning and end of the

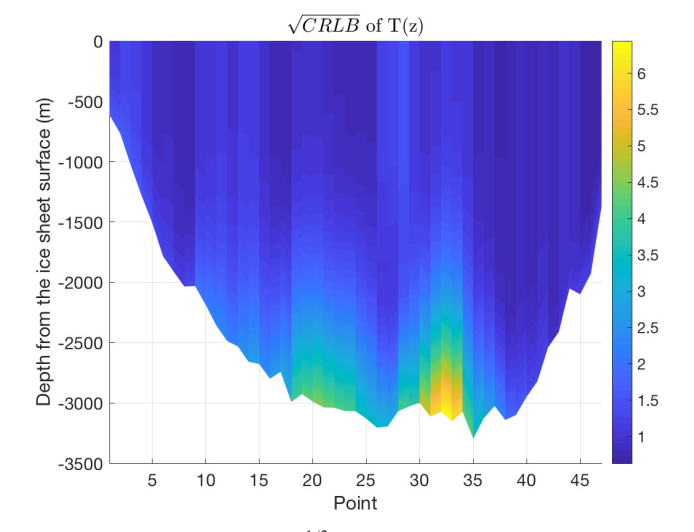


Fig. 5. Ice temperature $(CRLB)^{1/2}$ along the flight path at all depths.

flight path. In addition to the local minima solution, there are two possible explanations for this situation: mismatch in other parameter estimates that cause G to move away from the true value in compensation, or the greater thickness for this portion of the path. For additional examination, we performed a separate experiment with a geothermal heat flux prior specified to be further from the truth, referred to as the "degraded G" experiment hereafter. The G estimated in the degraded G experiment remained close to the prior estimation in locations where the ice is greater than 3 km thick, which suggests that while the surface of the ice sheet can be well interpreted with low-frequency microwave measurements, the basal situation of the ice sheet remains highly uncertain in the VE retrieval. It is also noted that in Fig. 7(a), Δ is consistently underestimated along the flight line. Intuitively, this underestimation may be compensating for estimation error in T_s and G. Further studies on the relationship of these three parameters are needed.

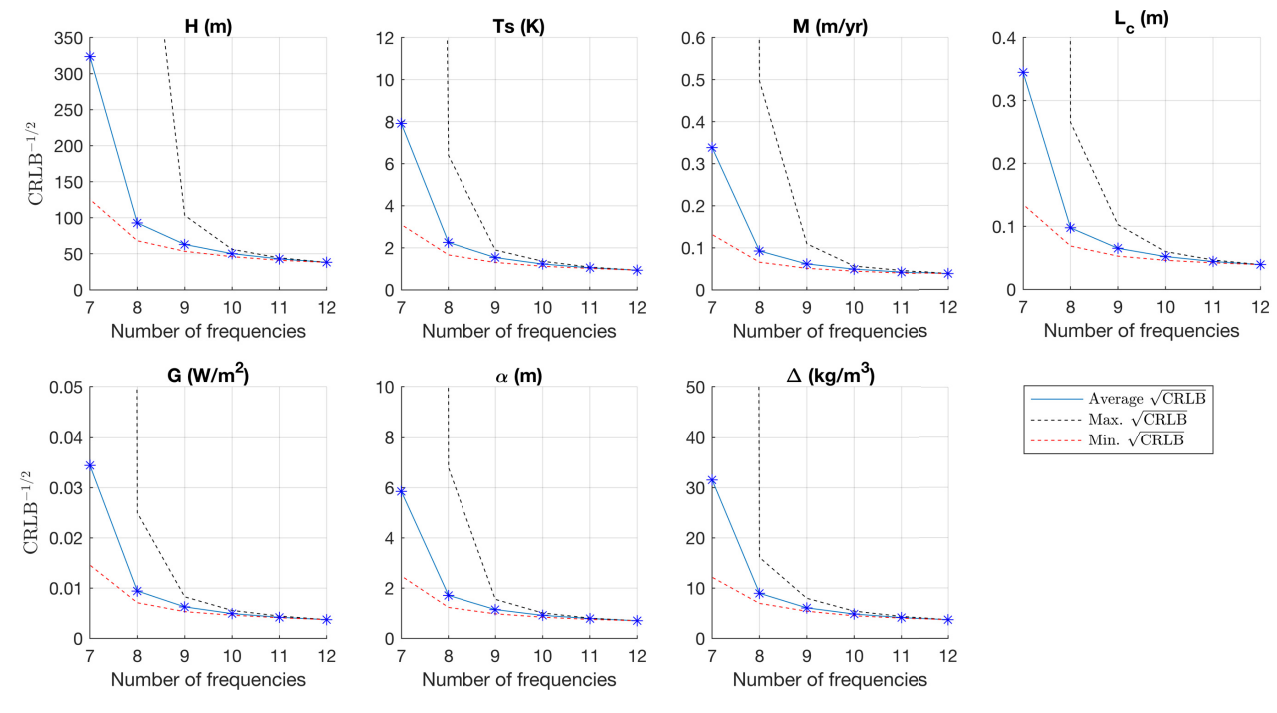


Fig. 6. Square root of the CRLB of ice sheet parameters as a function of the number of frequencies used.

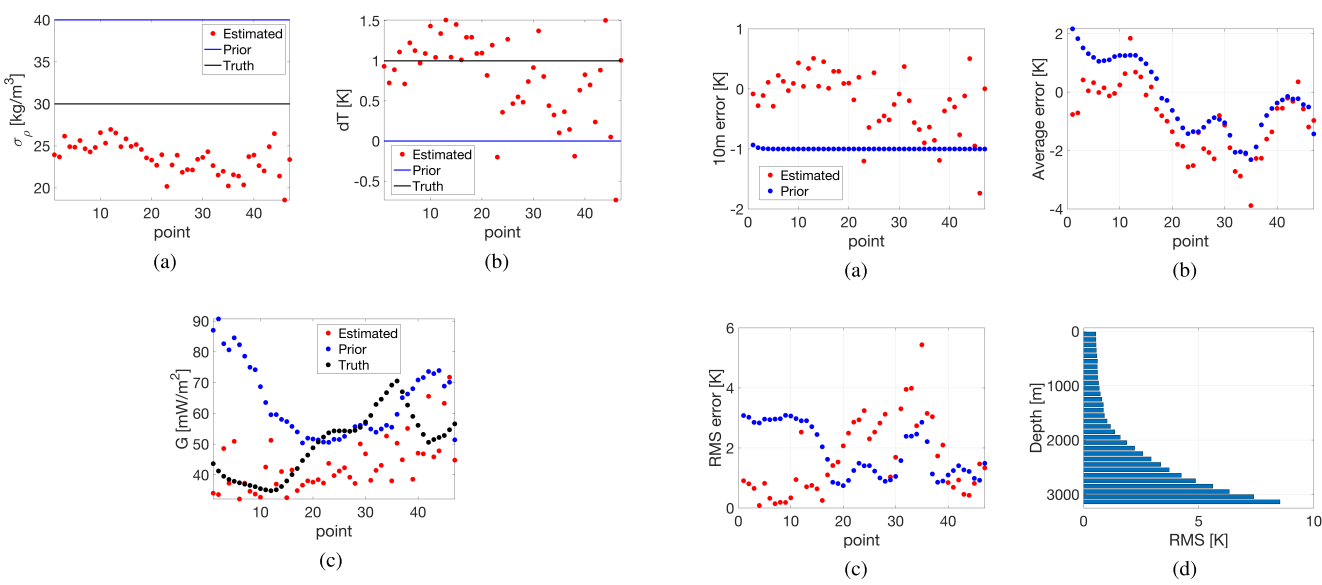


Fig. 7. VE estimates (red) of density variation, surface temperature, and geothermal heat flux along the nominal flight path compared with prior estimation and true value. (a) Fluctuation of density variation. (b) Surface temperature offset. (c) Geothermal heat flux.

Fig. 8. Error statistics of the MCMC temperature estimates. (a) 10 m temperature estimation error. (b) Average temperature estimation error. (c) Root mean square error of the temperature estimation. (d) RMS error of 100 m depth averaged temperature estimation error.

2) Vertical Temperature Profile Estimates: Fig. 8 shows the key three error statistics computed on the VE vertical temperature profile estimates. In Fig. 8(a), 10 m temperatures are all estimated to within 1 K, and mostly to within 0.5 K, despite the prior estimate having a precision of only 1.0 K. All 47 10 m temperature estimates showed improvement over the prior. In Fig. 8(b), the depth-averaged temperature estimates are constrained to within 2.5 K and mostly to within 2 K; the average error is within 1 K for the first 20 points along the flight path, roughly corresponding to ice thicknesses less than 3000 m. In Fig. 8(c), rms errors of the UWBRAD estimates are all within 3.3 K; 28 of the 47 points show improvement over the prior; rms errors are generally less than 1 K when the ice is

less than 3000 m thick. Both the average temperature estimates and the rms errors of the estimation showed improvements over the prior estimations at the beginning and end of the flight path. Fig. 8(d) shows all temperature estimate rms errors along the flight path based on 100 m depth increments; note that the rms for each bin is thus computed over a slightly different number of estimates. From Fig. 8(d), the estimation error increases with depth and stays below 1 K up to about 1500 m. This analysis emphasizes the role played by ice sheet thickness on retrieval accuracy.

3) Correlation Between Model Parameters: The correlation coefficient of the MCMC chains for the three parameters are

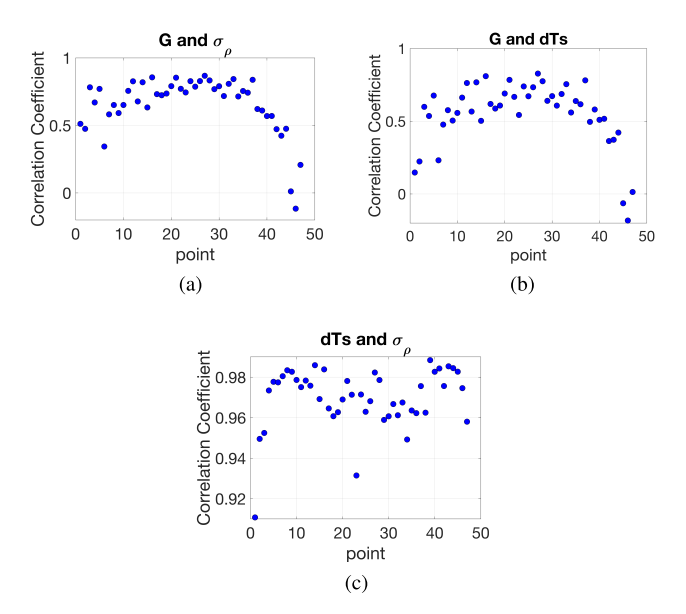


Fig. 9. Correlation coefficient between each of the three pairs of parameters. (a) Geothermal heat flux and fluctuation of density variation. (b) Geothermal heat flux and surface temperature. (c) Fluctuation of density variation and surface temperature.

calculated at each point and illustrated in Fig. 9. Along the flight line, a consistently high correlation of over 0.95 between surface temperature and density variations is observed in Fig. 9(c), which means that multiple combinations of density variations and surface temperatures in the sample space would produce the same T_b . Despite the high correlation between these two parameters, the 10 m temperature remains accurately estimated and shows significant improvement over the prior estimate. Correlation between the other two pairs of parameters shown in Figs. 9(a) and 9(b) are still relatively high (up to approximately 0.8 in some cases), but are much lower than those shown in Fig. 9(c). Note that the correlation is greatest for ice thicker than 3000 m. Highly correlated geophysical parameters can result in poor MCMC/estimation performance and can be addressed by reparametrization using coordinate rotation [33].

We further explore the correlation between dT_s and Δ in Fig. 10. Fig. 10(a) shows all the samples in the Markov chain excluding the burn-in period for the first point along the flight path, with three particular samples highlighted. The T_b spectra for the three highlighted samples are plotted in Fig. 10(b), along with the synthetic observation. The corresponding spectral difference for each sample is 3.11 K for blue, 3.05 K for cyan, 4.21 K for red, and 3.92 K for black. The sample with the coldest T_s and lowest value of Δ has the largest spectral difference in Fig. 10(b) (shown in red in all three plots), but the level of noise in the synthetic observation makes extracting such information challenging; note that all four T_b spectra are fairly similar. The temperature profiles generated with each set of parameters for the three highlighted samples are plotted in Fig. 10(c) along with the true temperature profile. It can be observed in Fig. 10(a) that for the three selected points, Δ varies from about 35 to 50 kg/m³. As Δ increases from 35 (red) to 40 kg/m³(blue), it is slightly over the true value of 30 kg/m³ and thus "pushes" the simulated T_b away from the truth. Consequently, the surface temperature increases about 5 K to compensate the loss as Δ continues to increase to

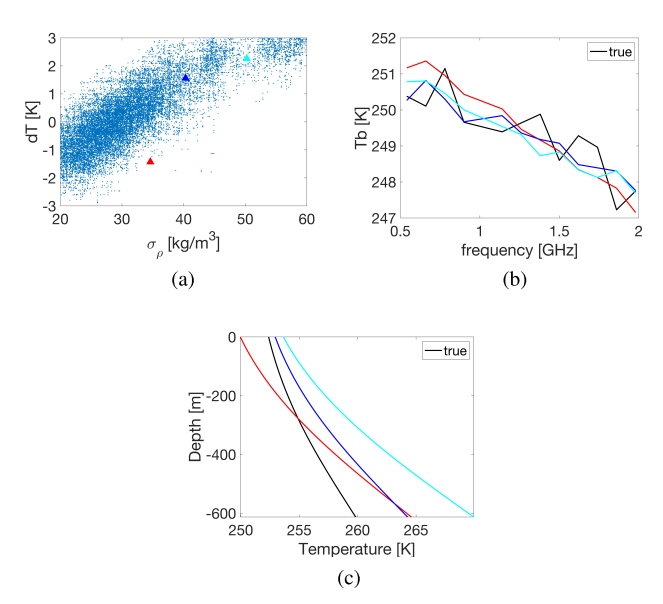


Fig. 10. MCMC chains reveal the relationship between parameter estimates for the first point along the flight path. (a) Markov chain samples for dT and Δ . The three highlighted samples are indicated by triangle markers. (b) T_b profiles for the three highlighted samples. (c) T_i vertical profiles for the three highlighted samples.

TABLE I
ERROR STATISTICS OF THE MCMC ESTIMATION WITH
DIFFERENT OBSERVATION ERROR

Observation	Mean 10m	Mean Average	Mean RMS
error	error	error	error
0.5K	0.0743	-0.4529	1.0741
2K	-0.1052	-0.3678	1.4037
3K	-0.1478	-0.4085	1.6544
5K	-0.4762	-0.5822	1.8148

about 50 kg/m 3 (cyan), which is further beyond the true value. The surface temperature alone fails to compensate for the T_b offset while maintaining a reasonable value. The geothermal heat flux is therefore then adjusted to constrain the temperature profile jointly. The use of additional prior information in the estimation scheme in future work may help to resolve some of these parameter dependencies.

4) Sensitivity to Observation Error: In previous experiments, the observation error was specified as 0.5 K. The VE T_i error statistics corresponding to the science goals averaged over the entire flight path for various observation error levels are presented in Table I. It is promising to see that even when the observation is ten times larger than the original experiment, the rms error averaged over 47 points increases only from 1.07 to 1.81 K. The MCMC process is still capable of producing a correct estimation even under fairly severe observation degradation.

Estimations using the data obtained between Camp Century-NEEM-NGRIP in [32] compares well with these results with roughly 1 K estimation rms error with a noise temperature of 1 K, similar to the values reported in Table I.

5) Effects of Robin Model: The Robin model assumes steady state heat transfer while in reality, the seasonal variation and paleoclimatic events would be recorded within the ice sheet and cause fluctuations in the upper part of the in situ measured temperature profile [17]. As the Robin model is not capable of including this upper layer variation, use of the model introduces additional uncertainty into the T_i estimates.

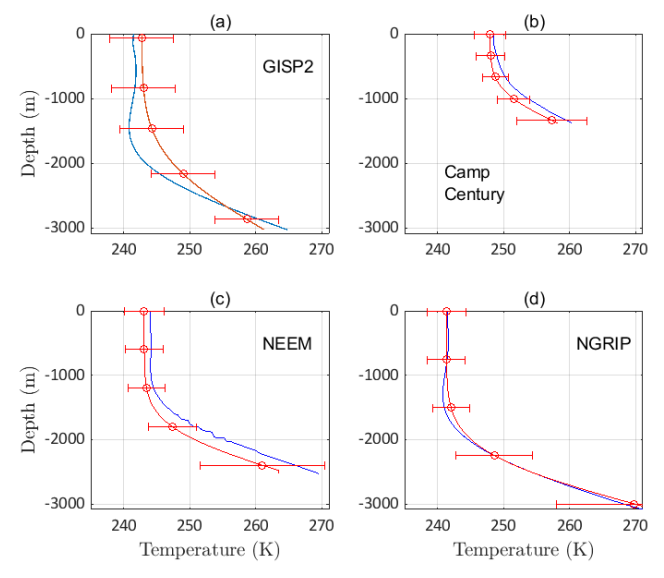


Fig. 11. Bayesian temperature estimation results for (a) GISP2, (a) Camp Century, (c) NEEM, and (d) NGRIP. Borehole data (blue) versus UWBRAD estimate (red) along with $\pm 2\sigma$ error bars using (a) simulated, (b)–(d) real data.

The result of the experiment described above using the borehole T_i as the basis for generating synthetic observations is shown in Fig. 11(a). The 10 m estimation and average estimation error are 0.27 and 1.57 K, respectively. The rms error is 2.16 K with the maximum error of -3.84 K occurred at the depth of 1951 m. Thus, the additional uncertainty introduced by the Robin model is of the same approximate magnitude as the error levels presented above.

Boreholes at three other locations along the flight path, namely Camp Century, NEEM, and NGRIP, were also shown in Fig. 11(b)–(d). These are the good candidates for dry ice with no horizontal drift or other processes so Robin model works well for these three locations. Actual data from [32] are used in the Bayesian estimation for these locations. The estimated profile and two standard deviation error bars (corresponding to 95% confidence interval) are also provided. Results show that UWBRAD has the potential to achieve the three main goals provided in Section I.

However, current formulation indeed limits the application of UWBRAD to regions where Robin is valid. Using more accurate models such as [34] or [35] it should be possible to extend the validity region to cover all Greenland and Antarctica.

V. DISCUSSION

It is remarkable that multispectral low-frequency measurements of microwave emission near L-band carry information on ice temperature profiles. This study presents a detailed analysis characterizing that information. We showed in simulation for Greenland, the 10 m temperature can be estimated to high precision, but that T_i vertical profiles for ice greater than 3000 m in thickness is more challenging to estimate, meaning that it is challenging but possible to achieve 1 K precision for average and rms of the vertical temperature profile across the entire Greenland ice divide. Note that these conclusions are specific to Greenland, because the dielectric properties and penetration depth are sensitive to ice temperature, and thus should be interpreted with care.

We also show that T_b observation precision is critical, with T_i uncertainty increasing when the T_b uncertainty is greater than 2 K. This is a challenging precision target to hit, due to RFI, as well as the general challenge of operating of airborne radiometers in very cold environmental conditions. Nonetheless, there are good reasons for optimism regarding the ability of UWBRAD observations to infer ice temperatures. First, we find that these results are essentially consistent between two completely different analyses, the CRLB and VE using an MCMC algorithm. The CRLB shows that the best achievable precision falls within the desired science goals, in most cases, while the VE demonstrates a particular algorithm capable of achieving that precision. Second, both analyses use minimal or no prior information: the CRLB uses no prior information at all, whereas the MCMC prior is assumed to follow a uniform distribution, and is thus relatively uninformative. Use of additional observational datasets, and Gaussian or other prior estimates of the forward model parameters may yield higher precision estimates, even if the UWBRAD observation precision is coarser than that considered here. Also, comparing the accuracies of the retrieved temperature related parameters with the ones of different systems commonly used for each parameter, the retrieval framework performed well in improving the knowledge of those parameters. For example, for T_s , It is claimed that the average bias of satellite-derived and in situ ice-surface temperature is well within the rms error of 2.1 K [36]. While for the UWBRAD, the CRLB provided that the T_s can be obtained with a standard deviation of 0.8 K. Another good example will be the retrieval of G as the Geothermal heat flux is largely unknown. Two geothermal heat flux models are frequently used for Greenland: one inferred from seismic tomography and the other from magnetic [37]. Maule et al. [14] claims the uncertainty of the magnetic anomalies derived geothermal heat flux data is 0.021-0.027 W/m² in Antarctica. The results in CRLB shows that geothermal heat flux can be estimated with standard deviation better than 0.005 W/m^2 .

VI. CONCLUSION

We find that both the CRLB and VE analyses support the conclusion that UWBRAD T_b observations can be used to infer T_i profiles at precisions high enough to enable new scientific understanding of the Greenland ice sheet. In particular, the 10 m temperature has been shown to be retrievable with the desired precision, despite the challenges of disentangling the effects of temperature and ice density variations on the microwave emission. For ice deeper than approximately 3000 m, the precision of the retrievals is degraded but overall goals of the system can still be satisfied as shown in [32]. Observation precision is an important control on final T_i precision, but even in the case of fairly high T_b uncertainty, our experiments indicate there is significant information in the observations. The results shown here with no prior (for the CRLB) or with a noninformative prior (for the VE) are useful in establishing the information content in the UWBRAD observations. Use of more informative priors is expected to improve the estimates. Thus, measurements of microwave emission near L-band carry information on ice temperature profiles, in agreement with the conclusions of Jezek et al. [3]. This work lays a more formal basis for confidence in UWBRAD temperature observations derived from

real airborne observations, and thus supports new scientific findings of temperature dynamics within ice sheets using this unique measurement technique.

ACKNOWLEDGMENT

The authors would like to thank the Ohio State Supercomputer Center for their support in the high-performance computing resources during this study [38].

REFERENCES

- [1] C. Mätzler, Thermal Microwave Radiation: Applications for Remote Sensing, vol. 52. Edison, NJ, USA: IET, 2006.
- [2] E. M. Morris and D. G. Vaughan, "Snow surface temperatures in West Antarctica," Antarctic Sci., vol. 6, no. 4, pp. 529-535, Dec. 1994.
- [3] K. C. Jezek et al., "Radiometric approach for estimating relative changes in intraglacier average temperature," IEEE Trans. Geosci. Remote Sens., vol. 53, no. 1, pp. 134-143, Jan. 2014.
- [4] G. Macelloni, M. Leduc-Leballeur, F. Montomoli, M. Brogioni, C. Ritz, and G. Picard, "On the retrieval of internal temperature of Antarctica ice sheet by using SMOS observations," Remote Sens. Environ., vol. 233, Nov. 2019, Art. no. 111405.
- [5] G. Macelloni, M. Leduc-Leballeur, M. Brogioni, C. Ritz, and G. Picard, "Analyzing and modeling the SMOS spatial variations in the east Antarctic plateau," Remote Sens. Environ., vol. 180, pp. 193-204, Jul. 2016.
- [6] S. Tan et al., "Physical models of layered polar firn brightness temperatures from 0.5 to 2 GHz," IEEE J. Sel. Topics Appl. Earth Observ. Remote Sens., vol. 8, no. 7, pp. 3681–3691, Jul. 2015.
- [7] F. T. Ulaby, R. K. Moore, and A. K. Fung, Microwave Remote Sensing: Active and Passive, From Theory to Applications, vol. 3. Norwood, MA, USA: Artech House, 1986.
- [8] J. T. Johnson et al., "Measurements of 0.5-2 GHz thermal emission spectra from the Greenland ice sheet, sea ice, and permafrost: Results from September 2017 campaign," in Proc. IEEE Int. Geosci. Remote Sens. Symp., Jul. 2018, pp. 8525–8527.
 [9] M. J. Andrews et al., "The ultrawideband software-defined microwave
- radiometer: Instrument description and initial campaign results," IEEE Trans. Geosci. Remote Sens., vol. 56, no. 10, pp. 5923-5935, Oct. 2018.
- [10] R. Thomas et al., "Mass balance of the Greenland ice sheet at high elevations," *Science*, vol. 289, no. 5478, pp. 426–428, Jul. 2000. [11] I. Joughin and K. Jezek, "The Radarsat-1 mosaic data," 2007. [12] E. Van Meijgaard et al., *The KNMI Regional Atmospheric Climate Model*
- RACMO Version 2.1. De Bilt, The, Netherlands: Koninklijk Nederlands Meteorologisch Instituut, 2008.
- [13] C. Leuschen, P. Gogineni, F. Rodriguez-Morales, J. Paden, and C. Allen, Icebridge Mcords L2 Ice Thickness, Version 1. Boulder, CO, USA: NASA National Snow and Ice Data Center Distributed Active Archive Center, 2010, doi: 10.5067/GDQ0CUCVTE2Q.
- [14] C. F. Maule, M. E. Purucker, N. Olsen, and K. Mosegaard, "Heat flux anomalies in Antarctica revealed by satellite magnetic data," Science, vol. 309, no. 5733, pp. 464-467, Jul. 2005.
- [15] G. Granzow. (2012). Greenland Basal Heat Flux. [Online]. Available: http://websrv.cs.umt.edu/isis/index.php/1km_Greenland_data_set
- [16] M. Stuiver, P. M. Grootes, and T. F. Braziunas, "The GISP₂ δ 18O climate record of the past 16,500 years and the role of the sun, ocean, and volcanoes," Quaternary Res., vol. 44, no. 3, pp. 341-354, Nov. 1995.
- [17] G. D. Clow, "GISP2-D temperature. PANGAEA," 1999, doi: 10.1594/PANGAEA.55517
- [18] T. H. Shoji, K. Kawada, O. Watanabe, and H. Clausen, "An empirical relation between overburden pressure and firn density," Ann. Glaciol., vol. 20, pp. 87–94, 1994, doi: 10.3189/1994AoG20-1-87-94.
- [19] E. M. Morris and D. J. Wingham, "The effect of fluctuations in surface density, accumulation and compaction on elevation change rates along the EGIG line, central Greenland," J. Glaciol., vol. 57, no. 203, pp. 416-430, 2011.
- [20] E. Morris and K. Jezek, "T41 station neutron data near summit," 2014. [21] G. D. Q. Robin, "Ice cores and climatic change," Philos. Trans. Roy.
- Soc. London. B, Biol. Sci., vol. 280, no. 972, pp. 143-168, 1977 [22] C. Ritz, "Interpretation of the temperature profile measured at Vostok, east Antarctica," Ann. Glaciol., vol. 12, pp. 138-144, 1989, doi:

10.3189/S0260305500007102.

- [23] A. Salamatin, V. Lipenkov, and K. Blinov, "Vostok (Antarctica) climate record timescale deduced from the analysis of a boreholetemperature profile," Ann. Glaciol., vol. 20, pp. 207-214, 1994, doi: 10.3189/1994AoG20-1-207-214.
- [24] J. MacGregor et al., "A synthesis of the basal thermal state of the Greenland ice sheet," J. Geophys. Res., Earth Surface, vol. 121, no. 7, pp. 1328-1350, 2016.

- [25] L. Tsang, T. L. Wang, J. T. Johnson, K. C. Jezek, and S. R. Tan, "A partially coherent microwave emission model for polar ice sheets with density fluctuations and multilayer rough interfaces from 0.5 to 2 GHz," in Proc. IEEE Int. Geosci. Remote Sens. Symp. (IGARSS), Jul. 2016, pp. 7082-7084
- [26] M. Brogioni, G. Macelloni, F. Montomoli, and K. C. Jezek, "Simulating multifrequency ground-based radiometric measurements at dome C-Antarctica," IEEE J. Sel. Topics Appl. Earth Observ. Remote Sens., vol. 8, no. 9, pp. 4405-4417, Sep. 2015.
- [27] R. D. West, D. P. Winebrenner, L. Tsang, and H. Rott, "Microwave emission from density-stratified Antarctic firn at 6 cm wavelength," J. Glaciol., vol. 42, no. 140, pp. 63-76, 1996.
- [28] M. Brogioni, S. Pettinato, F. Montomoli, and G. Macelloni, "Snow layering effects on L-band passive measurements at dome C-Antarctica," in Proc. 13th Specialist Meeting Microw. Radiometry Remote Sens. Environ. (MicroRad), Mar. 2014, pp. 61-64.
- [29] S. M. Kay, Fundamentals of Statistical Signal Processing: Estimation Theory, vol. 1. Upper Saddle River, NJ, USA: Prentice-Hall, 1993.
- [30] A. Gelman, J. B. Carlin, H. S. Stern, and D. B. Rubin, Bayesian Data Analysis. Boca Raton, FL, USA: Chapman & Hall, 1995, ch. 11.2 Metropolis and Metropolis-Hastings Algorithms, pp. 320–344. [31] D. K. Hall, J. C. Comiso, N. E. DiGirolamo, C. A. Shuman, J. R. Key,
- and L. S. Koenig, "A satellite-derived climate-quality data record of the clear-sky surface temperature of the Greenland ice sheet," J. Climate, vol. 25, no. 14, pp. 4785–4798, Jul. 2012. [32] C. Yardim et al., "Greenland ice sheet subsurface temperature estima-
- tion using ultrawideband microwave radiometry," IEEE Trans. Geosci. Remote Sens., vol. 60, pp. 1-12, 2022.
- [33] C. Yardim, P. Gerstoft, and W. S. Hodgkiss, "Estimation of radio refractivity from Radar clutter using Bayesian Monte Carlo analysis," IEEE Trans. Antennas Propag., vol. 54, no. 4, pp. 1318–1327, Apr. 2006, doi: 10.1109/TAP.2006.872673.
- [34] S. Rezvanbehbahani, C. J. Veen, and L. A. Stearns, "An improved analytical solution for the temperature profile of ice sheets," J. Geophys. Res., Earth Surf., vol. 124, no. 2, pp. 271-286, Feb. 2019.
- [35] H. Seroussi, M. Morlighem, E. Rignot, A. Khazendar, E. Larour, and J. Mouginot, "Dependence of century-scale projections of the Greenland ice sheet on its thermal regime," J. Glaciol., vol. 59, no. 218, pp. 1024-1034, 2013.
- [36] D. K. Hall, J. E. Box, K. A. Casey, S. J. Hook, C. A. Shuman, and K. Steffen, "Comparison of satellite-derived and in-situ observations of ice and snow surface temperatures over Greenland," Remote Sens. Environ., vol. 112, no. 10, pp. 3739-3749, Oct. 2008.
- [37] N. Shapiro, "Inferring surface heat flux distributions guided by a global seismic model: Particular application to Antarctica," Earth Planet. Sci. Lett., vol. 223, nos. 1–2, pp. 213–224, Jun. 2004. (1987). Ohio Supercomputer Center. [Online]. Available: http://osc.edu/
- ark:/19495/f5s1ph73



Yuna Duan received the B.S. degree from Hohai University, Nanjing, China, in 2014. She is currently pursuing the Ph.D. degree with the School of Earth Science, The Ohio State University, Columbus, OH, USA.

Her research interests include passive microwave remote sensing of snow, Bayesian modeling, and thermal dynamics of glaciers.



Caglar Yardim (Member, IEEE) received the Ph.D. degree in electrical engineering from the University of California at San Diego, La Jolla, CA, USA, in 2007.

He was a Scientist at the Marine Physical Laboratory, Scripps Institution of Oceanography, La Jolla, until 2014. He is currently a Research Assistant Professor with the ElectroScience Laboratory (ESL), Electrical and Computer Engineering Department, The Ohio State University (OSU), Columbus, OH, USA. He is also the Head of the Atmospheric

and Oceanographic Electromagnetics and Marine Systems Laboratory, ESL-OSU. His research interests include atmospheric propagation, nonstandard atmospheric conditions, remote sensing, numerical electromagnetic (EM) techniques, radar, clutter modeling, microwave radiometry, applied signal processing, Bayesian techniques, adaptive beamforming, interferometry, underwater acoustics, and seismics.



Michael Durand received the B.S. degree in mechanical engineering and biological systems engineering from the Virginia Polytechnic Institute, Blacksburg, VA, USA, in 2002, and the M.S. and Ph.D. degrees in civil engineering from the University of California at Los Angeles, Los Angeles, CA, USA, in 2004 and 2007, respectively.

He is currently an Associate Professor with the Byrd Polar and Climate Research Center, School of Earth Sciences, The Ohio State University, Columbus, OH, USA.



Kenneth C. Jezek received the B.S. degree in physics from the University of Illinois Urbana–Champaign, Urbana, IL, USA, in 1973, and the M.S. and Ph.D. degrees in geophysics from the University of Wisconsin–Madison, Madison, WI, USA, in 1977 and 1980, respectively, where he studied the behavior of the Ross Ice Shelf Antarctica using ice sounding radar data collected during several visits to the Antarctic.

He was in charge of the McMurdo Station, Antarctica Cosmic Ray Laboratory, Ross Island,

Antarctica, in winter 1974. Before joining OSU's Byrd Polar Research Center as the Director in 1989, he was a Geophysicist with the U.S. Army Cold Regions Research and Engineering Laboratory, Hanover, NH, USA, where he researched the electromagnetic (EM) and acoustical properties of sea ice in the laboratory and in the Arctic. He also served a two-year term as the Manager for the NASA's Polar Oceans and Ice Sheets Program. From 1997 to 2007, he led the Radarasat Antarctic Mapping Project. From 2007 to 2010, he was Co-Leader of the International Polar Year Global Inter-agency International Polar Snapshot Year (GIIPSY) Project which involved the participation of 12 space agencies. He has chaired the Land Ice Science Team for NASA's Operation Icebridge from 2010 to 2013. He is a Professor Emeritus at the Byrd Polar Research Center, School of Earth Sciences, The Ohio State University (OSU), Columbus, OH, USA.



Joel T. Johnson (Fellow, IEEE) received the bachelor's degree in electrical engineering from the Georgia Institute of Technology, Atlanta, GA, USA, in 1991, and the S.M. and Ph.D. degrees from the Massachusetts Institute of Technology, Cambridge, MA, USA, in 1993 and 1996, respectively.

He is currently a Professor with the Department of Electrical and Computer Engineering and the ElectroScience Laboratory, The Ohio State University, Columbus, OH, USA. His research interests include microwave remote sensing and propagation,

and electromagnetic (EM) wave theory.

Dr. Johnson is a member of Commissions B and F of the International Union of Radio Science (URSI), Tau Beta Pi, Eta Kappa Nu, and Phi Kappa Phi. He received the Best Paper Award from the IEEE Geoscience and Remote Sensing Society in 1993, was named an Office of Naval Research Young Investigator, received the National Science Foundation Career Award and the Presidential Early Career Award for Scientists and Engineers (PECASE) Award in 1997, and was recognized by the U.S. National Committee of URSI as a Booker Fellow in 2002.



Shurun Tan (Member, IEEE) received the B.E. degree in information engineering and the M.Sc. degree in electromagnetic (EM) field and microwave techniques from Southeast University, Nanjing, China, in 2009 and 2012, respectively, and the Ph.D. degree in electrical engineering from the University of Michigan, Ann Arbor, MI, USA, in 2016.

From December 2010 to November 2011, he was a Visiting Student with the Department of Electrical and Computer Engineering, The University of Houston, Houston, TX, USA. From September 2012

to December 2014, he was a Ph.D. Student with the Department of Electrical Engineering, University of Washington, Seattle, WA, USA. From January 2015 to December 2018, he was with the Radiation Laboratory and the Department of Electrical Engineering and Computer Science, University of Michigan, Ann Arbor, first as a Ph.D. Student, and then as a Post-Doctoral Research Fellow since January 2017. He is currently an Assistant Professor with Zhejiang University/University of Illinois at Urbana-Champaign Institute, International Campus of Zhejiang University, Haining, China. He is also with the State Key Laboratory of Modern Optical Instrumentation and the College of Information Science and Electronic Engineering, Zhejiang University, Hangzhou, China. He is an Adjunct Assistant Professor with the Department of Electrical and Computer Engineering, University of Illinois at Urbana-Champaign, Urbana, IL, USA. He is working on EM theory, computational, and applied EMs. His research interests include EM scattering of random media and periodic structures, microwave remote sensing, EM information systems with EM wavefunctional devices, EM integrity in highspeed and high-density electronic integration, EM environment, and reliability of complex electronic systems.



Leung Tsang (Life Fellow, IEEE) received the B.S., M.S., and Ph.D. degrees from the Massachusetts Institute of Technology, Cambridge, MA, USA, in 1983.

From 1983 to 2014, he was a Professor at the University of Washington, Seattle, WA, USA, where he was the Chair of the Department of Electrical Engineering from 2006 to 2011. From 2001 to 2004, he was a Professor at the City University of Hong Kong, Hong Kong. He is currently a Professor with the Department of Electrical Engineering and

Computer Science, University of Michigan, Ann Arbor, MI, USA. He has coauthored *Theory of Microwave Remote Sensing and Scattering of Electromagnetic Waves* (volumes 1–3). His research interests include remote sensing, waves in random media, rough surfaces, electromagnetic (EM) theory, computational EM, signal integrity, EM compatibility, and plasmonics.

Dr. Tsang was the President of the IEEE Geoscience and Remote Sensing Society from 2006 to 2007. He received the William Pecora Award co-sponsored by the United States Geological Survey (USGS) and NASA in 2012, and the IEEE Electromagnetics Award in 2013. He is on the Editorial Board of IEEE Access and is the Chair of the Progress in Electromagnetics Research (PIERS).



Alexandra Bringer received the M.S. and Ph.D. degrees in physics from the Universite du Sud-Toulon-Var, La Garde, France, in 2009 and 2012, respectively.

She joined the Electroscience Laboratory, The Ohio State University, Columbus, OH, USA, for a post-doctoral position in 2014, where she is currently a Senior Research Associate. Her studies were focused on physical oceanography and remote sensing. She is involved in microwave radiometry for cryosphere applications and radio

frequency interference detection and mitigation. Her research interests include microwave remote sensing, ocean and cryosphere remote sensing, and signal processing.



Mustafa Aksoy (Member, IEEE) received the B.S. degree in electrical and electronics engineering from Bilkent University, Ankara, Turkey, in 2010, and the M.S. and Ph.D. degrees in electrical engineering from The Ohio State University, Columbus, OH, USA, in 2014 and 2015, respectively.

He was a Post-Doctoral Research Associate at the Joint Center for Earth Systems Technology, University of Maryland Baltimore County, Baltimore, MD, USA, and at the NASA Goddard Space Flight Center, Lanham, MD, USA. He is currently an

Assistant Professor with the Department of Electrical and Computer Engineering, University at Albany, SUNY, Albany, NY, USA. His research interests include microwave remote sensing, electromagnetic (EM) theory, and signal processing.